

NH₃ Observations of the Infrared Dark Cloud G28.34+0.06

Y. Wang^{1,2}, Q. Zhang², T. Pillai^{2,3}, F. Wyrowski³, Y. Wu¹,

ABSTRACT

We present observations of the NH₃ (J,K) = (1,1) and (2,2) inversion transitions toward the infrared dark cloud G28.34+0.06, using the Very Large Array. Strong NH₃ emission is found to coincide well with the infrared absorption feature in this cloud. The northern region of G28.34+0.06 is dominated by a compact clump (P2) with a high rotation temperature (29 K), large line width (4.3 km s⁻¹), and is associated with strong water maser (240 Jy) and a 24 μm point source with far IR luminosity of 10³ L_⊙. We infer that P2 has embedded massive protostars although it lies in the 8 μm absorption region. The southern region has filamentary structures. The rotation temperature in the southern region decreases with the increase of the integrated NH₃ intensity, which indicates an absence of strong internal heating in these clumps. In addition, the compact core P1 in the south has small line width (1.2 km s⁻¹) surrounded by extended emission with larger line width (1.8 km s⁻¹), which suggests a dissipation of turbulence in the dense part of the cloud. Thus, we suggest that P1 is at a much earlier evolutionary stage than P2, possibly at a stage that begins to form a cluster with massive stars.

Subject headings: clouds - ISM: kinematics and dynamics -stars: formation

¹Astronomy Department and CAS-PKU Joint Beijing Astrophysics Center, Peking University, Beijing 100871, P.R.China

²Harvard-Smithsonian Center for Astrophysics, Cambridge, MA 02138, U.S.A.

³Max-Planck-Institut für Radioastronomie, Auf dem Hügel 69, D-53121 Bonn, Germany

1. Introduction

Stars form from the collapse of dense molecular gas and dust. While low-mass stars tend to form in isolation and small groups, high-mass stars ($M > 8 M_{\odot}$) are born almost exclusively in clusters (Lada & Lada 2003). The process of low-mass star formation in the isolated environment is relatively well studied (Shu, Adams & Lizano 1987). However, the processes through which gas and dust condense to assemble massive stars and clusters are poorly understood. Klessen (2004) and Mac Low (2004) proposed that, in large scales, the supersonic turbulence provides the support to the cloud, while, in small scales, density enhancements cause gravitational collapse. And Myers (1998) and Goodman et al. (1998) also proposed that, after the turbulence dissipation, gas condensation will lose internal support against the gravity to form stars. Such scenario requires observational tests in massive regions where clouds are very likely to form massive stars and clusters. Studies of massive infrared dark clouds (IRDCs) can provide such opportunities.

Infrared dark clouds are the dark patches in the sky revealed in the infrared wavelengths against the bright galactic background. Surveys along the galactic plane using the Infrared Space Observatory (ISO) and the Midcourse Space Experiment (MSX) identified thousands of extinction features at $8 \mu\text{m}$ (Egan et al. 1998; Hennebelle et al. 2001; Simon et al. 2006). Their spatial coincidence with emission from molecular lines and dust indicates that these dark clouds consist of dense molecular gas and dust of $n_{H_2} \sim 10^5 \text{ cm}^{-3}$ (Carey et al. 1998, 2000). Temperatures in these clouds are low enough (10–20 K) that they do not radiate significantly even at the mid or far infrared wavelength. The large amount of dense gas and dust in these clouds make them the natural birth place for clusters (Carey et al. 1998, 2000; Johnstone et al. 2003; Rathborne et al. 2005, 2006, 2007; Teyssier, Hennebelle & Pérault 2002; Redman et al. 2003; Pillai et al. 2006a,b; Sridharan et al. 2005; Beuther et al. 2005).

However, most of the previous studies focus on IRDCs that already have strong star formation activities (e.g. Rathborne et al. 2005), and thus, are at a more evolved evolutionary stage. In addition, due to the large distances to these objects, observations with single dish telescopes do not have sufficient spatial resolution to reveal the substructures in massive clumps and variations of physical parameters. Using the Very Large Array, we imaged a giant infrared dark cloud, G28.34+0.06 at high angular resolution. The object of interest is a good target to search for molecular clumps in an early evolutionary stage. At a distance

of ~ 4.8 kiloparsecs (kpc), it contains about $10^3 M_{\odot}$ of dense gas in the infrared absorption region (Carey et al. 2000; Rathborne et al. 2006). The NH_3 observations with the Effelsberg 100m telescope show that, on average, its line width is smaller than those obtained in high mass protostellar objects and Ultracompact HII (UCHII) regions, and the gas temperature is lower than 20 K (Pillai et al. 2006b). In our VLA observations, the temperature structure and line width variations indicate that the northern region of G28.34 harbors massive protostellar objects, while, in the southern region, the clumps have characteristics of the earliest phase of star formation.

2. Observations

We observed the NH_3 (J, K) = (1,1) line at 23.694 GHz and the (2,2) line at 23.723 GHz with the VLA of the NRAO¹ on 2004 June 15 in its D configuration. Seven pointings were observed to cover the extended emission; each pointing has an on-source integration time of 12 minutes and covers a FWHM primary beam of $2'$. We used the 4IF mode that splits the 256-channel correlator into four sections to allow simultaneous observations of the NH_3 (1,1) and (2,2) lines with two circular polarizations for each line. The channel separation used was 48.8 KHz ($\sim 0.6 \text{ km s}^{-1}$ at the line frequency). The time variation of the gains was calibrated by quasar, 1851+005, observed at a cycle of ~ 20 mins. The absolute flux density is established by bootstrapping to 3C286. The bandpass is calibrated via observations of 3C84.

The visibility data sets were calibrated and imaged using the AIPS software package of the NRAO. The average rms of the final images is $\sim 3 \text{ mJy/beam}$ per 48.8 KHz wide channel. The synthesis beam is about $3'' \times 5''$ when using the natural weighting of the visibilities. In order to recover extended structures missing in the interferometer data, we combined the visibility data from the VLA with the Effelsberg 100m single dish data from Pillai et al. (2006b) for both the NH_3 (1,1) and (2,2) lines following the Miriad procedure outlined in Vogel et al. (1984).

¹The National Radio Astronomy Observatory is operated by Associated Universities, Inc., under cooperative agreement with the National Science Foundation.

3. Results and Discussions

3.1. General Properties

Fig. 1 presents the integrated intensity of the NH_3 (1,1) line from the combined data set overlaid on the $8 \mu\text{m}$ image obtained from the Galactic Legacy Infrared Mid-Plane Survey Extraordinaire (GLIMPSE; PI: Churchwell) using the Infrared Array Camera (IRAC). The dense gas traced by NH_3 follows the $8 \mu\text{m}$ absorption feature very well. Several compact clumps are revealed in the filamentary structure. These clumps also coincide with the 1.2 mm dust continuum emission obtained from the IRAM 30m telescope (Rathborne et al. 2006).

In the region north of $\delta_{(2000)} < -04:00:45$ (hereafter the Northern Region), both the NH_3 and 1.2 mm emission are centrally peaked with a dust mass of $\geq 600 M_\odot$ (Carey et al. 2000). There exists an HII region associated with IRAS 18402-0403, but has little NH_3 or 1.2 mm emission. The $24 \mu\text{m}$ image from the 24 and 70 Micron Survey of the Inner Galactic Disk with MIPS (MIPSGAL; PI: Carey) reveals five embedded point sources. IRS 3 coincides with IRAS 18402-0403, and has a luminosity of $10^3 L_\odot$ (Carey et al. 2000). IRS 2 is detected toward the 1.2mm continuum peak P2, and is associated with the NH_3 peak and a strong H_2O maser (240 Jy). Its luminosity of $10^3 L_\odot$ based on the Spitzer data from 3.6 to $70 \mu\text{m}$ and 1.2mm flux, and a lack of cm emission suggest a high-mass protostellar object. The remaining three $24 \mu\text{m}$ sources have luminosities of $10^2 L_\odot$.

The region south of $\delta_{(2000)} < -04:00:45$ (hereafter the Southern Region) has no detectable emission at 1.3cm at an rms of 0.7 mJy, and is associated with three H_2O masers (Wang et al. 2006). Both the NH_3 and 1.2mm emission have a flatter spatial distribution, with a total mass over $1500 M_\odot$ (Rathborne et al. 2006). Four $24 \mu\text{m}$ sources are detected from the MIPSGAL survey with luminosities $< 10^2 L_\odot$. The strongest source, IRS 1 ($\alpha_{(2000)}=18:42:50.82$ $\delta_{(2000)}=-04:03:09$) with a luminosity of $10^2 L_\odot$, is associated with an NH_3 peak toward P1 ($\alpha_{(2000)}=18:42:50.27$ $\delta_{(2000)}=-04:03:20$), and an H_2O maser emission ($\alpha_{(2000)}=18:42:50.80$ $\delta_{(2000)}=-04:03:11.0$). The other two H_2O masers in the Southern Region has no $24 \mu\text{m}$ sources within a projected distance of $30''$.

It is difficult to predict whether the Southern Region will eventually form

massive stars similar to the Northern Region. The Southern Region contains more dense molecular gas than the Northern Region. Assuming a similar star forming efficiency, one would expect a more massive cluster to emerge in the Southern Region. **However, since the south is spatially more extended, it may form less massive stars than the Northern Region. On the other hand, if the cluster follows a normal Salpeter IMF, one would expect more massive stars in the Southern Region.** Thus, a lack of luminous infrared sources in the south indicates that it is at an earlier evolutionary stage than the Northern Region. Furthermore, the radio data in conjunction with the infrared data appear to suggest an evolutionary sequence of star formation, starting with an evolved stage in IRAS 18402-0403/IRS3; to an embedded phase in IRS2 which has a luminosity similar to high-mass protostellar objects; to less luminous IRS1 which has strong mm continuum, and H₂O maser emission; and finally to NH₃ clumps which only has strong mm continuum emission, but no 24 μ m emission peak nor H₂O maser emission.

The NH₃ data reveal physical properties that further confirm the difference in the Northern and Southern Region. In the Northern Region, there is a dominant compact clump P2 associated with IRS 2 ($\alpha_{(2000)}=18:42:51.92$ $\delta_{(2000)}= -03:59:54$), which has a peak rotation temperature close to 30 K and a FWHM line width larger than 3 km s⁻¹, and is surrounded by an extended envelope. By averaging rotation temperatures in the Northern Region of the same NH₃ (1,1) intensities, we derived a relation between the two quantities. Fig. 2 presents the average NH₃ temperature within an intensity bin versus the mean value of the bin. As shown in the black line in Fig. 2, the rotation temperature in the Northern Region increases with the increase of the integrated intensity, which indicates strong internal heating in clump P2 of the Northern Region. Therefore, although clump P2 is embedded in the 8 μ m dark region, the high temperature, large line width, strong water maser, and 24 μ m point source indicate that this compact clump is forming massive protostellar object(s), similar to the compact cores found in other IRDCs (Pillai et al. 2006a; Rathborne et al. 2005, 2007; Beuther et al. 2005).

On the other hand, the NH₃ emission from the Southern Region appears to have different characteristics as compared to that in the Northern Region. The red line in Fig. 2 shows that the rotation temperature in the Southern Region decreases with the increase of the integrated NH₃ intensity. On average, areas with stronger NH₃ emission have lower temperatures, which

indicates absence of strong internal heating in the southern clumps, unlike P2 in the north. Toward the most compact clump P1/IRS1 in the Southern Region, the NH_3 gas has a lower rotation temperature (~ 16 K) and narrower line width (~ 1.8 km s $^{-1}$) than that in P2. We also note that the temperature decrease appears to flatten toward the highest intensity in the red line in Fig. 2. This could be due to the limited heating from star formation activities in the area.

We also compared the general properties of G28 Southern Region with the local, intermediate mass star formation region OMC-north (Bally et al. 1987; Hillenbrand 1997; Castets & Langer 1995; Johnstone & Bally 1999). The linear resolution of our interferometer and single dish combined NH_3 image ($\sim 4''$ resolution) of G28.34+0.06 (distance of ~ 4.8 kpc) is comparable with the Effelsberg 100m single dish NH_3 image ($40''$ resolution) of the OMC-north (distance of ~ 0.48 kpc) (Cesaroni et al. 1994). We found that, on average, G28.34 Southern Region have lower temperatures (16 K vs. 20 K), larger line width (1.6 vs 0.8 km s $^{-1}$) and higher column density (2.3 vs. 0.78×10^{22} cm $^{-2}$) assuming the same NH_3 abundance (0.3×10^{-7}) in both regions. The mass within the dense filament estimated from dust emission is $\sim 1500 M_\odot$ in G28.34-south region (Rathborne et al. 2006), while the dense mass in OMC-north is $\sim 350 M_\odot$ (Lis et al. 1998). On the other hand, G28.34-south region extends $4'$ (~ 6 pc) at the distance of ~ 4.8 kpc, while OMC-north extends $20'$ (~ 3 pc) at the distance of ~ 0.48 kpc. All these parameters indicate that G28.34-south has colder and more turbulent dense gas packed in a smaller region than OMC-north.

3.2. Line Width Variation of NH_3 Emission toward Peaks P1 and P2

We examined the spatial variation of NH_3 (1,1) line width from the VLA data as well as that combined with the Effelsberg 100m single dish data. The line width variations after the data combination provide kinematic information on the scale of ≥ 0.1 pc ($4''$ in 4.8 kpc). The line width of P1 and P2 before and after the data combination are shown in Table 1. It appears that the line width in P1 is broader after adding the single dish data, while, in P2, we find an opposite effect. Since the missing flux in an interferometer corresponds to the extended spatial structures, the variation in the line width represents a change in the level of turbulence in their envelopes/cores along the line of sight. Normally, in a typical

active massive star forming core, such as P2, the missing fluxes in an interferometer are from extended and quiescent envelopes. Dense and compact emission surrounding high mass protostars or UCHII regions has broader line width due to motions such as infall, outflow and rotation. The missing extended structures are normally weaker and have narrower line width. However, toward the G28.34 Southern Region, we observed the opposite effect: the extended emission shows systematically larger line widths than those from the compact core component revealed by interferometer.

This effect is also shown in line width distribution in Fig. 3. The line width distribution appears to behave differently in the clumps from the Northern and Southern region after data combination. As shown in Fig. 3, for the cold clump P1 in the Southern Region, the mean line width becomes broader after recovering the missing flux, while for the warm clump P2, the mean line width is similar to the one from the interferometer data alone. Furthermore, the line widths of the entire Southern Region follow a distribution similar to P1. We find that the effect of relative motions among clumps can be ruled out. We tested this scenario by convolving the combined interferometer data to the resolution of the single dish telescope (40''), and comparing with the line width of the combined data at 4'' resolution. The mean line widths from these two data sets are similar.

The variations of NH_3 line width in the G28 Southern Region suggest a dissipation of turbulence, possibly at the onset of star/cluster formation. The dissipation of turbulence could initiate gravitational collapse as suggested by several observations (e.g. Ward-Thompson, D., 2002). Taking advantage of the high resolution of interferometers, we obtained the line width variation of P1 and P2 along the line of sight on scales of ≥ 0.1 pc. Using the NH_3 data, we calculated the molecular mass and virial mass (Estalella et al. 1993) of P1 and P2 (Table 1). In P1, the material seen from both interferometer alone and the combined data sets is gravitationally bound. And the dense component is more likely to collapse ($M = 16 M_\odot$ vs. $M_{vir} = 6 M_\odot$) than the component including all the spatial structures ($M = 27 M_\odot$ vs. $M_{vir} = 14 M_\odot$). In contrast, due to strong star formation activities, the dense component in P2 has a larger virial mass ($75 M_\odot$) than the molecular mass ($30 M_\odot$), while the whole clump is gravitationally bound and may undergo collapse ($M = 75 M_\odot$ vs. $M_{vir} = 44 M_\odot$). We suggest that, in the cold massive clump P1, and the rest of the G28.34-south region, dense gas undergoes fragmentation and condensation. Considering the low rotation

temperature (~ 16 K), relatively narrow line width (~ 1.8 km s $^{-1}$), P1 appears to be in a very early evolutionary stage during which turbulence dissipates to facilitate gravitational collapse to form stars. At this stage of cluster/massive star formation, the most massive members in the cluster may be still at the intermediate mass stage, and will likely continue to accrete to become more massive stars, given the amount of dense gas available in the region.

We thank referee D. Johnstone for his constructive comments. This research is supported by the Grant 10128306 and 10733030 of NSFC and G1999075405 of NKBRFSF. This work is based in part on observations made with the *Spitzer Space Telescope*, which is operated by the Jet Propulsion Laboratory, California Institute of Technology. We would like to thank the GLIMPSE team (PI: E. Churchwell) and MIPS GAL team (PI: S. Carey) for making the IRAC and MIPS images available to the community. The authors also gratefully acknowledge Mr. Keping Qiu's help in reducing the MIPS data.

REFERENCES

- Beuther, H.; Sridharan, T. K.; Saito, M. 2005, ApJ, 634, L185
- Carey, S. J., Clark, F. O., Egan, M. P., et al. 1998, ApJ, 508, 721
- Carey, S. J., Feldman, P. A., Redman, R. O., et al. 2000, ApJ, 543, L157
- Castets, A., Langer, W. D., 1995, A&A, 294, 835
- Cesaroni, R., Wilson, T. L. 1994, A&A, 281, 209
- Di Francesco, J., Andre, P, Myers, P. C., 2004, ApJ, 617, 425
- Egan, M. P., Shipman, R. F., Price, S. D., et al. A Population of Cold Cores in the Galactic Plane. 1998, ApJ, 494, L199
- Estalella, R., Mauersberger, R., Torrelles, J. M., Anglada, G., Gomez, J. F., Lopez, R. & Muders, D. 1993, ApJ, 419, 698
- Hennebelle, P., Perault, M., Teyssier, D., Ganesh, S, 2001, A&A, 365, 598

- Hillenbrand, Lynne A., 1997, *AJ*, 113, 1733
- Johnstone, Doug; Bally, John. 1999, *ApJ*, 510, 49
- Johnstone, Doug; Fiege, Jason D.; Redman, R. O.; Feldman, P. A.; Carey, Sean J., 2003, *ApJ*, 588, 37
- Klessen, Ralf S., 2004, *Ap&SS*, 292, 215
- Lada, Charles J., Lada, Elizabeth A., 2003, *ARA&A*, 41, 57
- Larson, R. B. 1985, *MNRAS*, 214, 379
- Lis, D. C., Serabyn, E., Keene, Jocelyn, Dowell, C. D., Benford, D. J., Phillips, T. G., Hunter, T. R., Wang, N., 1998, *ApJ*, 509, 299
- MacLow, Mordecai-Mark, 2004, *Ap&SS*, 289, 323
- Mouschovias, T. C. 1991, *ApJ*, 373, 169
- Myers, P. C., 1998, *ApJ*, 496, L109
- Pillai, T., Wyrowski, F., Carey, S.J., & Menten, K.M., 2006a, *A&A*, 447, 929
- Pillai, T., Wyrowski, F., Menten, K.M., & E.Krugel, 2006b, *A&A*, 450, 569
- Rathborne, J. M., Jackson, J. M., Chambers, E. T., Simon, R., Shipman, R., Frieswijk, W., 2005, *ApJ*, 630, L181
- Rathborne, J. M., Jackson, J. M., Simon, R., 2006, *ApJ*, 641, 389
- Rathborne, J. M., Simon, R., Jackson, J. M., 2007, *ApJ*, 662, 1082
- Redman, R. O., Feldman, P. A., Wyrowski, F., Cote, S., Carey, S. J., Egan, M. P., 2003, *ApJ*, 586, 1127
- Shu, Frank H., Adams, Fred C., Lizano, Susana, 1987, *ARA&A*, 25, 23
- Simon, R., Jackson, J. M., Rathborne, J. M., Chambers, E. T., 2006, *ApJ*, 639, 227
- Teyssier, D., Hennebelle, P., Prault, M., 2002, *A&A*, 382, 624

Sridharan, T. K., Beuther, H., Saito, M., Wyrowski, F., Schilke, P., 2005, ApJ, 634, L57

Vogel, S. N., Bieging, J. H., Plambeck, R. L., Welch, W. J., Wright, M. C. H., 1984, ApJ, 283, 655

Ward-Thompson, Derek. 2002, Sci.,295, 76.

Wang, Y., Zhang, Q., Rathborne, J. M.; Jackson, J & Wu, Y., 2006, ApJ, 651, L125

Fig. 1.— The integrated intensity of the combined NH_3 (1,1) emission in white solid contours overlaid on the Spitzer $8\ \mu\text{m}$ image in logarithmic color scales. The NH_3 image is contoured at 10% of the peak ($1\ \text{Jy beam}^{-1} \times \text{km s}^{-1}$). The star symbols mark the $24\ \mu\text{m}$ emission peaks observed with MIPS/*Spitzer*. The cross symbols mark water maser emission detected with the VLA. The thin dashed line indicates the 50% of the sensitivity level of the 7 pointing mosaic in NH_3 . The NH_3 data have a resolution of $5'' \times 3''$, shown as the shaded ellipse at the lower-left corner of the panel.

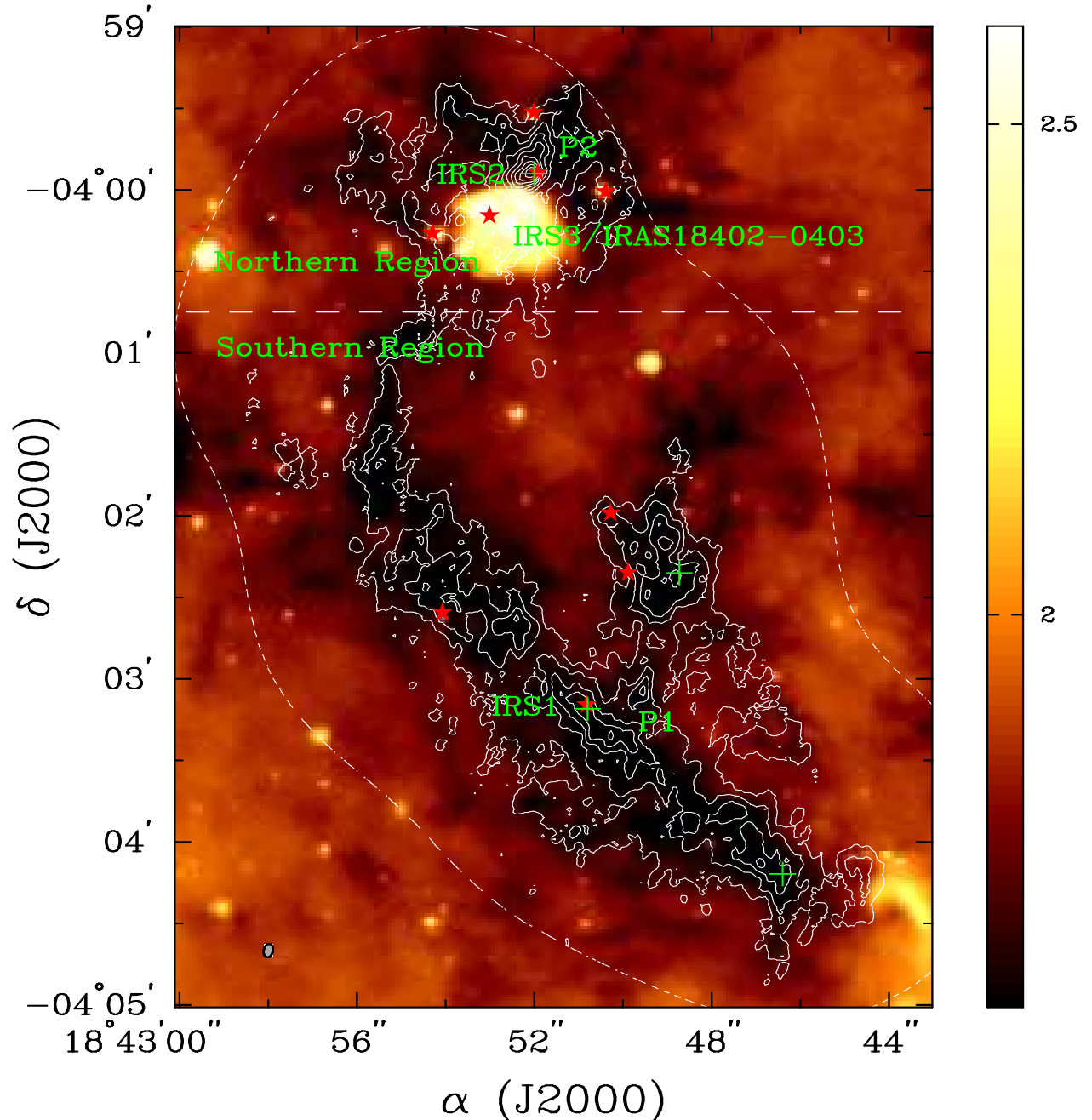


Fig. 2.— Relation between rotation temperature and NH_3 (1,1) integrated intensity in the Northern Region (black) and the Southern Region (red) of G28.34+0.06. The error bars present the 1σ standard deviation.

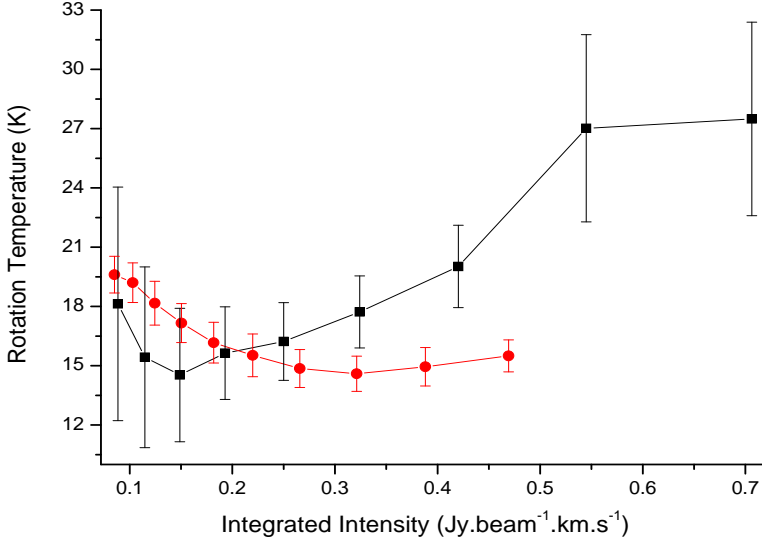


Fig. 3.— NH_3 (1,1) line width distribution in different velocity bins toward G28.34+0.06. Red columns are the number count from the VLA data set. Green columns are the number count from the combined data set (VLA+100m). **Left:** Line width distribution for clump P2 over an area of $10'' \times 10''$. **Right:** Line width distribution for clump P1 over an area of $15'' \times 5''$. The NH_3 line widths, measured in FWHM, are corrected for optical depth and broadening due to hyperfine structures.

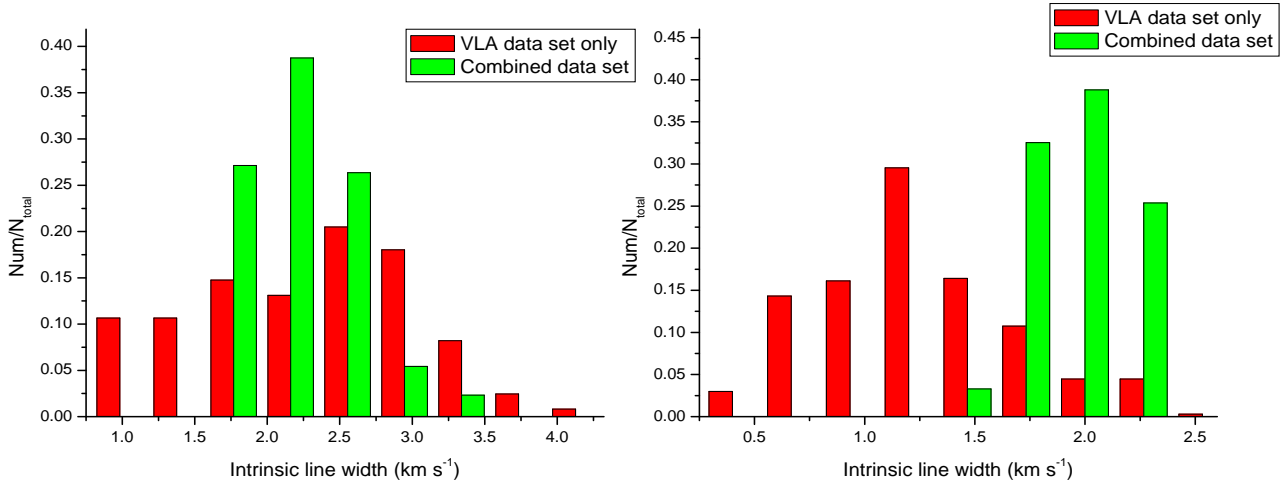


Table 1. Physical Parameters of P1 and P2 over the Scale of 0.1 pc

Source Name	R.A. (2000)	DEC. (2000)	Δv^a (km s ⁻¹)	N_{col}^a (10 ¹⁶ cm ⁻²)	Mass ^a (M _⊙)	Virial Mass ^a (M _⊙)	NH ₃ Abundance ^b (10 ⁻⁷)
P1 ^c	18 42 50.27	-04 03 20	1.2/1.8	0.59/1.0	16/27	6/14	0.6
P2 ^c	18 42 52.07	-03 59 54	4.3/3.3	0.48/1.2	30/75	75/44	0.3

Note. — Units of right ascension are hours, minutes, and seconds, and units of declination are degrees, arcminutes, and arcseconds.

^aThe first number is obtained from the VLA data only; The second number is obtained from the combined data.

^bThe NH₃ abundance is calculated by comparing the column density of dust (Rathborne et al. 2006) and NH₃ emission. We convolved the NH₃ data to 11'', the the resolution of the dust emission, and assumed that the NH₃ abundance is the same in (11'' × 11'').

^cThe coordinates of P1 and P2 refer to the integrated intensity peaks of combined NH₃ (1,1) data.